ADVANCED PHOTONICS RESEARCH
www.adpr-journal.com

Phenothiazine–Quinoline Conjugates Realizing Intrinsic Thermally Activated Delayed Fluorescence and Room-Temperature Phosphorescence: Understanding the Mechanism and Electroluminescence Devices

*Nirmalya Acharya, Monirul Hasan, Suvendu Dey, Shih-Chun Lo, Ebinazar B. Namdas, and Debdas Ray**

Understanding the local triplet (^{3}LE), charge transfer triplet (^{3}CT), and charge transfer singlet (^{1}CT) is of great importance in designing thermally activated delayed fluorescence (TADF) and room-temperature phosphorescence (RTP) materials for their use in organic light-emitting devices (OLEDs), sensing, and bioimaging. Herein, two phenothiazine–quinoline conjugates (PTzQ1, PTzQ2) in which the donor (PTz) and acceptor (Q1, Q2) parts are held in near-orthogonal orientation that gives rise to spatial separation of the highest occupied molecular orbital (HOMO) and lowest unoccupied molecular orbital (LUMO) are reported. Photophysical studies of both conjugates along with their individual components (PTz, Q1, Q2) show that TADF occurs via reverse intersystem crossing (rISC) from the upper-level local triplet (^{3}LE) to lower-level singlet ^{1}CT mediated by vibronic coupling between ^{3}LE and ^{3}CT, whereas RTP is realized from ^{3}LE. It is found that all three excited states are close in energy, 0.16–0.19 eV (^{3}LE$-^1$CT), 0.02–0.03 eV (^{1}CT$-^3$CT), and 0.14–0.16 eV (^{3}LE$-^3$CT) with the order of $^3\text{LE} > {}^1\text{CT} > {}^3\text{CT}$. Both conjugates exhibit a high rate constant of rISC (k_{rISC}, 7.9–9.7 $\times 10^5$ s^{-1}), resulting in external quantum efficiency (EQE) values of ≈4.7% (solution processed) with emission from both RTP and TADF components.

1. Introduction

Electroluminescent devices are now established as light sources for display and lighting applications due to their high efficiency and long lifetimes. They rely on a layer of electroluminescent material sandwiched between two electrodes. Recombination of injected charges leads to the formation of an excited state that emits light, known as electroluminescence (EL).[1] According to spin statistics, recombination of the injected holes and electrons produces singlet and triplet excitons in a 1:3 ratio,[1] and modern light-emitting devices (LEDs) harness both singlet and triplet excitons to achieve high efficiency using transition-metal-based phosphorescent complexes. Efficient phosphorescence from the triplet excited state of organometallic systems, typically iridium complexes, has been widely investigated, and 100% internal quantum efficiency (IQE) was achieved due to the use of heavy metals that allow strong spin–orbit coupling (SOC) for efficient intersystem crossing (ISC).[2] Despite their high IQE, these systems suffer from degradation related to the population of higher-lying $^3dd^*$ metal orbitals,[3] instability issues,[4] and cost effectiveness. Therefore, an alternative approach to substituting organometallic phosphors by cheaper organic materials is highly desirable. It is well known that organic molecules have typically low ISC and low-phosphorescence rate constants ($k_p < 10^2$ s^{-1}), which render them much less efficient compared with traditional heavy metal-based systems,[2d,e] although a recent study of heavy-atom-free room-temperature phosphorescent organic light-emitting

N. Acharya, S. Dey, Dr. D. Ray
Advanced Photofunctional Materials Laboratory
Department of Chemistry
Shiv Nadar University
NH-91, Gautam Buddha Nagar, Tehsil Dadri, Uttar Pradesh 201314, India
E-mail: debdas.ray@snu.edu.in

The ORCID identification number(s) for the author(s) of this article can be found under https://doi.org/10.1002/adpr.202000201.

DOI: 10.1002/adpr.202000201

M. Hasan, Dr. S.-C. Lo, Dr. E. B. Namdas
Centre for Organic Photonics and Electronics
The University of Queensland
Brisbane, QLD 4072, Australia

M. Hasan, Dr. E. B. Namdas
School of Mathematics and Physics
The University of Queensland
Brisbane, QLD 4072, Australia

Dr. S.-C. Lo
School of Chemistry and Molecular Biosciences
The University of Queensland
Brisbane, QLD 4072, Australia

diodes (OLEDs) has been established.[2f] In addition, organic molecules with localized nature of the triplet states show dim phosphorescence as it is very sensitive to thermal energy and the presence of oxygen. Recently, organic donor–acceptor (D–A)-based emitters that show thermally activated delayed fluorescence (TADF),[5] resulting via reverse intersystem crossing (rISC) from the lowest triplet (T_1) to the lowest singlet (S_1) state, have displayed 100% IQE by harvesting of both S_1 and T_1 excitons. In these systems, to enable spin upconversion from T_1 to S_1 by rISC, a low energy gap (ΔE_{ST}) (typically < 0.5 eV) between S_1 and T_1 has been established. It has been observed that spatial separation of the highest occupied molecular orbital (HOMO) and the lowest unoccupied molecular orbital (LUMO) of such emitters results in low ΔE_{ST} due to angular orientation of electron donor and acceptor parts. Further, TADF materials with D–A or D–A–D structure show intramolecular charge transfer (CT) states caused by D and A coupling. Recent experimental studies and quantum chemical calculations ensure that ISC and rISC between ^{1}CT singlet and ^{3}LE triplet states are mediated by vibronic coupling of the ^{3}CT to the locally excited triplet (^{3}LE) states to allow SOC to the ^{1}CT state,[6] which accelerates the rate constant of rISC (k_{rISC}).[7]

According to second-order perturbation theory, k_{rISC} can be expressed as

$$k_{rISC} = \frac{2\pi}{\hbar}\left|\frac{\psi^1_{CT}|\hat{H}_{SOC}|\psi^3_{LE}\psi^3_{LE}|\hat{H}_{vib}|\psi^3_{CT}}{\delta(E^3_{LE}-E^3_{CT})}\right|^2 \delta(E^3_{LE}-E^1_{CT}) \quad (1)$$

where $\psi^1(x)$ and $\psi^3(x)$ are the wave functions of ^{1}CT, ^{3}LE, and ^{3}CT, respectively. H_{SOC} and H_{vib} are the spin–orbit and vibrational Hamiltonians. It turns out that efficient rISC involves nonadiabatic coupling between the lowest triplet states (^{3}LE–^{3}CT) and SOC between the lowest ^{1}CT and ^{3}LE states (^{1}CT–^{3}LE). Hence, the best TADF is expected when the energy (E) levels of these three states are almost degenerate ($E_{1_{CT}} \approx E_{3_{CT}} \approx E_{3_{LE}}$).[6d,e]

On the other hand, to harvest triplet excitons via TADF with room-temperature phosphorescence (RTP) feature, a very good energy-level tuning of these three excited states should occur at ambient conditions.[8] Designing such organic systems is a difficult task as purely organic materials are intrinsically incapable of efficient phosphorescence at ambient conditions due to fast nonradiative decay pathways (k_{nr}) of the excited states,[9] although many design principles which rely on intra- and/or intermolecular interactions (lp•••π, π•••π, hydrogen bonding),[10] aggregates,[11] host–guest chemistry,[12] deuteration,[13] and the presence of heavy elements[14] in the molecular backbone have been developed. Recently, few researchers demonstrated simultaneous TADF and RTP from single molecular systems using chemical modification,[15] mechanical force,[8b,16] conformational switching,[17] and change of host matrices.[18] Despite these achievements, a proper understanding of the excited-state energy-level ordering ($E_{1_{CT}}, E_{3_{CT}}, E_{3_{LE}}$) of such dual emitters remains largely unclear. Therefore, such systems should be discovered to unravel the underlying mechanism that can find potential applications in OLEDs[5] and sensing.[19]

Previously, we have demonstrated how dual RTP and TADF can be achieved. Inspired by these studies,[8] we designed phenothiazine(D)–quinoline(A) conjugates (**Figure 1**) with the aim of efficient TADF with RTP due to well-matched excited energy levels (^{3}LE, ^{1}CT, ^{3}CT). Here, we designed two new systems by modifying electron donor groups onto the acceptor part of the naphthyl-appended phenothiazine(D)–quinoline(A) conjugates (PTzQ1, PTzQ2) without changing the donor part. Taking a cue from previous literature reports by Monkman and coworkers,[6d,e] where the phenothiazine (PTz)-based D–A and/or D–A–D systems show very weak coupling between the D and A parts at the ground state due to near-orthogonal orientation, we hypothesized that the covalently attached PTz part to the substituted quinolinyl ring via C–N single bond can adapt such twisted geometry that can lead to efficient TADF caused by vibronic coupling between the ^{3}LE and ^{3}CT and SOC between ^{1}CT and ^{3}LE states. The naphthyl unit was selected to avoid aggregate-caused quenching effect due to intermolecular π•••π interactions between the neighboring molecules. Furthermore, we imagine that such geometry can provide good control of excited energy ordering to enable RTP from the ^{3}LE state which is also responsible for TADF. Photophysical studies of both conjugates (films) revealed that TADF occurs via rISC between the upper-level locally triplet (^{3}LE) and lower-level singlet CT (^{1}CT) states mediated by ^{3}CT. We found high k_{rISC} of 0.91×10^7 s^{-1} (PTzQ1) and 0.84×10^7 s^{-1} (PTzQ2) in methyl cyclohexane solutions in inert atmosphere, which led to efficient TADF. We also observed that both conjugates showed green RTP from upper-level ^{3}LE to the ground state at ambient conditions. The energy difference, $\Delta E(^3\text{LE}-^3\text{CT})$ and $\Delta E(^3\text{LE}-^1\text{CT})$, were found to be 0.14–0.16 eV and 0.16–0.19 eV, respectively. Cyclic voltammetry (CV) measurements confirmed localization of HOMO and LUMO on the donor (PTz) and acceptor (Q1, Q2) parts. Single-crystal X-ray analysis (SCXRD) unambiguously confirmed that PTz and Q1 or Q2 parts of both conjugates are held in near-orthogonal orientation. Quantum chemistry calculations revealed that HOMO and LUMO of both conjugates are mainly distributed on the donor and acceptor parts, respectively, which gives rise to a singlet excited state with stronger CT characters with an electron promoted from the donor's HOMO to the acceptor's LUMO. Both compounds were used

Figure 1. Structure of the molecules (PTzQ1, PTzQ2) including two control compounds (Q1, Q2) synthesized in this study.

in solution-processed OLEDs to show peak external quantum efficiency (EQE) values of ≈4.7% (at 1 cd m^{-2}).

2. Results and Discussion

2.1. Synthesis

PTzQ1 and PTzQ2 were synthesized by the traditional nucleophilic aromatic substitution reaction (S_NAr) between phenothiazine and 1-fluoro-nitrobenzene, followed by a reduction of the nitrofunction to the amine intermediates, and treated with 1-ethynylnaphthalene and respective 4-substituted benzaldehydes in the presence of catalytic amount of iron(III)-trifluoromethanesulphonate in oxygenated conditions to obtain PTzQ1 and PTzQ2 (Figure 1, Scheme S1, Supporting Information). Control compounds (Q1, Q2) were synthesized by following the similar methodology using aniline. All the compounds were characterized by NMR spectroscopy, high resolution mass spectrometry (HRMS), and X-ray analysis (see Supporting Information).

2.2. X-Ray and CV Analysis

SCXRD of the two conjugates (PTzQ1, PTzQ2) revealed that the phenothiazine and naphthyl substituents attached to the C8 and C4 positions of the quinolinyl fragment deviate significantly from planarity (PTzQ1: 96.7 (5)°, −82.8 (7)°; PTzQ2: 98.64 (4)°, −103.9 (4)°), when viewed along the C(11A)—N(2)—C(8)—(9) and C(18)—C(17)—C(4)—C(3) atoms, respectively (**Figure 2**a,b, S9a,b, and Table S1, Supporting Information). However, the substituted phenyl rings connected to the C2 position of the quinolinyl ring is almost coplanar (PTzQ1, 0.8°; PTzQ2, 3.7(5)°) with the quinolinyl ring when viewed along the C32—C27—C2—N1 atoms, respectively. These twists around the N1—C8 and C4—C24 bonds in both molecules prohibit significant intramolecular conjugation. Figure 2a,b also shows that both conjugates have no crystallographic symmetry, and the phenothiazine (PTz) donors are folded by 22°/24° along **N•••S** vectors (Figure S9c,d, Supporting Information). We also found that the nonconjugated bond distances (N1—C8, N1—C11A) in the puckered PTz donor were found to be 1.411(5) Å (average) and 1.407(5) Å (average), respectively. Thus, PTz donors of both the conjugates adapt "quasiequatorial" conformation, which is consistent with the literature.[6d,e] In addition, X-ray analysis suggests that the intermolecular $\pi\cdots\pi$ interactions (4.2–4.4 Å) between the molecules (nearest π-centroid) (Figure S9e,f, Supporting Information) are not significant, which is also consistent with our hypothesis that the bulky naphthyl substituent can rule out the possibility of luminescence quenching in the solid state.

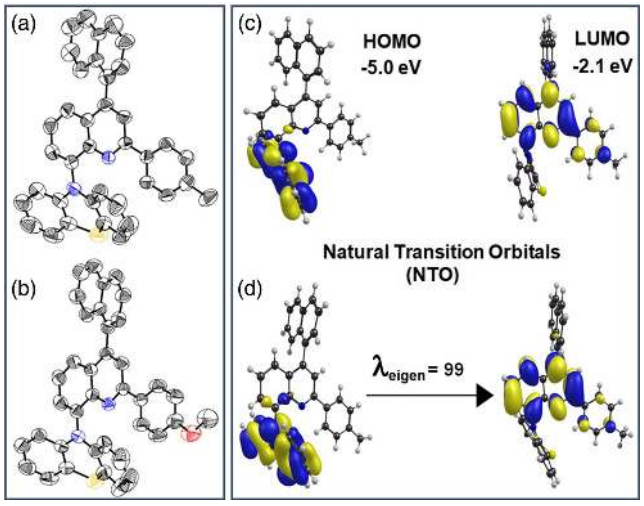

Figure 2. a) Oak Ridge thermal ellipsoid plots (50% probability ellipsoids) of a) PTzQ1 and b) PTzQ2. The protons are removed for the sake of clarity. c) HOMO and LUMO distribution and d) NTOs of PTzQ1 calculated for their first excited states.

CV measurements were carried out to understand their redox behaviors as well as the estimation of the HOMO and LUMO of both compounds and their individual donor and acceptor parts. The HOMO and LUMO energies are shown in Table S3 (Figure S10, Supporting Information), which are essentially consistent with the energy difference between the HOMO and LUMO levels of PTz and Q1 and/or Q2 (2.48, 2.47 eV) as determined by CV data. The results suggest that the HOMO–LUMO gaps in both conjugates are determined by the HOMO and LUMO levels of the donor and acceptor part and energies are largely localized on the donor (PTz) and acceptor (Q1 or Q2) parts of both the systems, which is in excellent agreement with the X-ray structures of both conjugates in which donor and acceptor are held in near-orthogonal arrangement.

2.3. Computational Analysis

We carried out quantum chemical calculations using density functional theory (DFT) in GAUSSIAN 09 D.01[20] at the B3LYP/6-311++G(d,p)[21] level of theory to gain a better insight into the molecular configuration and electronic structures of PTzQ1 and PTzQ2. The optimized molecular structures (gaseous state, crystal geometry) and the HOMO/LUMO distribution of the two compounds are shown in Figure 2c and S11, Supporting Information. The calculation showed that the HOMO is localized on the phenothiazine PTz moiety, whereas the LUMO is dominated by the quinolinyl ring of both conjugates, although a fair contribution is extended to the phenyl ring attached to the C2 position of the quinolinyl part. Such spatial overlap between the HOMO and LUMO suggests a strong CT transition and a small electron exchange energy. On the other hand, the dihedral angles between the donor (PTz) and acceptor (Q1/Q2) are found to be 96.7° and 97.2°, respectively, when viewed along the same atoms, which is fully consistent with X-ray analysis. The experimental transition energies for both conjugates are found to be an excellent match with time-dependent (TD)-DFT-calculated atomic transition energies (Figure S12, Supporting Information). The orbital transformation behavior from S_0 to S_1 atomic transition upon electronic excitation was obtained by calculating natural transition orbitals (NTO)[22] for both compounds (Figure 2d, and S11b, Supporting Information). The NTOs revealed that after electronic excitation the "hole" is localized on the electron donor PTz part, whereas the "particle" is distributed over quinoline ring with its phenyl substituent at 2-position. Hence, the existence of LE and CT states can be predicted from the

distribution of frontier orbitals and NTOs in electronic transitions. Thus, these analyses confirm our structural model in which the donor and acceptor are held in almost orthogonal orientation, which is key to achieve almost degenerate singlet–triplet levels promising for TADF and device study.

2.4. Thermal Analysis

The thermal properties of both conjugates, PTZQ1 and PTzQ2, are determined using thermogravimetric (TGA) and differential scanning calorimetry (DSC) analyses in nitrogen atmosphere (Figure S13, Supporting Information). DSC shows no glass transition temperature (T_g) during the second heating cycle, whereas melting peaks are observed at 258 and 203 °C, respectively. Further, TGA histograms of both compounds show primary decomposition (T_d, corresponding to 5% weight loss) at 352 and 390 °C, respectively. These excellent thermal properties ensure high morphologic stability of the amorphous phase in the film, which will be suitable for fabricating the high-thermally stable OLEDs.

2.5. Photophysics in Solutions

The ultraviolet–visible (UV–vis) absorption characteristics of the compounds were measured in solvents. **Figure 3**a shows the normalized UV–vis spectra of PTZQ1 and PTZQ2 as well as their individual donor (PTz) and acceptor (Q1 or Q2) parts, recorded in methyl cyclohexane (MCH) solvent (10 μM). Figure S14, Supporting Information, shows the absorption bands in solvents with different polarities. The lower-energy absorption peaks (PTzQ1: ≈350 nm; PTzQ2: ≈360 nm) of both conjugates are slightly red shifted with a broad tail as compared with the absorption bands of both donor (PTz) (320 nm, broad) and acceptor (Q1, Q2) (≈340–350 nm) parts, which can be ascribed to the electron-donating groups attached to Q1 and Q2, respectively, for conjugates. It is clear that the absorption spectra of both compounds are the total contributions of their donor and acceptor parts, indicating almost electronically decoupled systems. The lower-energy absorption bands (350–360 nm) with strong transition are assigned to the $\pi-\pi^*$ character as they remain unaffected by increasing polarity of the solvent.

Likewise, steady-state (SS) emission measurements of PTZQ1 and PTZQ2 (10 μM) were carried out in solvents of disparate polarities. In MCH, considering optical excitation of both PTz and Q1 (and/or Q2) parts ($\lambda_{ex} = 340$ nm), the structure-less emission peaks appeared at 561 nm (2.49 eV, onset) and 552 nm (2.55 eV, onset), for PTZQ1 and PTZQ2, respectively (Figure 3a). When we compare this emission feature with the individual components in nonpolar MCH, a significant bathochromic shift along with a parent weak emission (^{1}LE) at about 460 nm was observed for both PTZQ1 and PTZQ2 at ambient conditions, indicating that the radiative recombination from ^{1}LE can compete with electron transfer that populates the lower-energy ^{1}CT state (Figure 3a). It should be noted that the donor PTz emission band closely overlaps with the higher-energy emission band of the conjugates, which confirms that higher-energy emission band (460 nm) originates from the PTz unit.[6d,e] Further, this low-energy emission band is independent of λ_{ex}, which indicates that the CT occurs by excitation of both donor and acceptor parts (Figure S15a,b, Supporting Information). Furthermore, emission spectra of both the conjugates show bathochromic shift of the emission maxima with

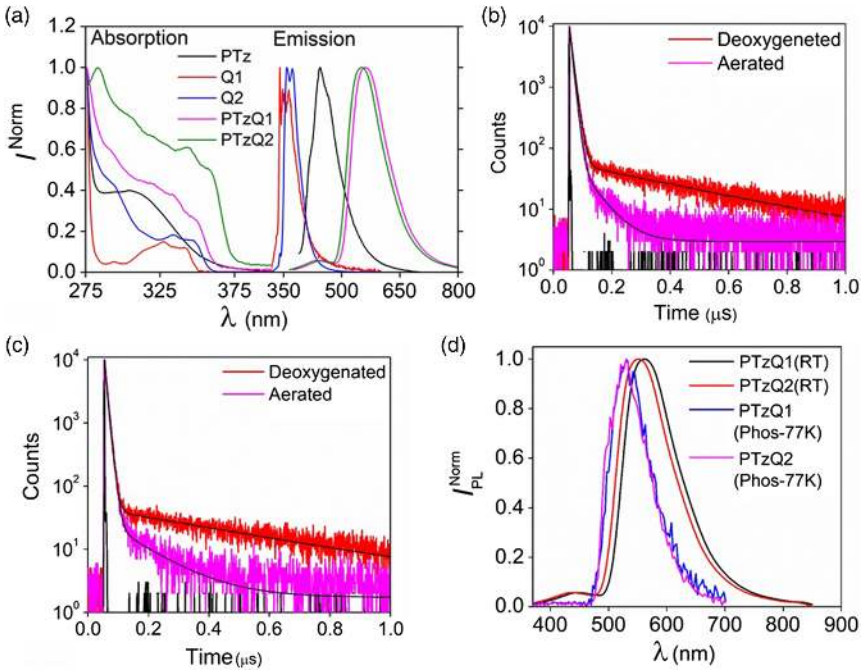

Figure 3. a) Solution absorption and emissions of PTzQ1, PTzQ2, Q1, and Q2 in methyl cyclohexane under ambient conditions (RT). Lifetime analysis of b) PTzQ1 and c) PTzQ2 in MCH under ambient and deoxygenated conditions. d) SS PL (RT) and phosphorescence (77 K) spectra of PTzQ1 and PTzQ2. Excitation wavelength = 340 nm (SS), 320 nm (lifetime).

broadband emission features (Gaussian peak) and reduction in the emission intensity with increase in polarity of the solvent (Figure S15c-f, Supporting Information). Such emissive states, which are typically observed in exciplex and twisted intramolecular CT states,[2d] are assigned as the ^{1}CT state, suggesting that the emission originates from an excited state with stronger CT characters. To understand the triplet state, the emission spectra of both compounds were recorded in aerated and deoxygenated MCH solutions at room temperature (RT). We found that both photoluminescence (PL) intensity and PL quantum yield (PLQY) in degassed solutions increase substantially (PLQY, from ≈10–$12 \pm 2\%$ to 38–$40 \pm 2\%$) and all the emission spectra overlap with each other, indicating that a triplet state is involved for emission, which relaxes radiatively from the same singlet ^{1}CT state (Figure S14, Supporting Information). At 300 K, both conjugates in degassed MCH solutions show biexponential trainset decay feature (PTzQ1: $\lambda_{em} = 561$ nm, $\tau_{PF} = 10.82$ ns, $\tau_{DF} = 0.42$ µs; PTzQ2: $\lambda_{em} = 552$ nm, $\tau_{PF} = 8.32$ ns, $\tau_{DF} = 0.51$ µs) (Figure 3b,c). The fast decay of the second component (sub-µs regime) indicates efficient rISC and hence, strong TADF, which is highly sensitive at ambient conditions. The delayed fluorescence (DF)/prompt fluorescence (PF) ratio determined from SS oxygen-dependent experiments was calculated to be 2.8 and 3.4, respectively, which is consistent with the typical TADF dyes (Figure S16, Supporting Information). Further, temperature-dependent PL measurements showed gradual increase in lifetime of the delayed component with increasing temperature from 210 to 300 K (Figure S17, and Table S4, Supporting Information). These results confirm that both conjugates harvest triplet states via TADF. Further, phosphorescence spectra were measured at 77 K. Interestingly, the phosphorescence bands (530 nm, 2.59 eV, onset) with full width half maximum (FWHM, 80-85 nm) of both the conjugates, which are locally excited (LE) in nature, are blue shifted (≈20 nm) as compared with the SS spectra recorded in MCH at RT (Figure 3d). To verify the origin of the triplet state, phosphorescence spectra of PTz, Q1, and Q2 were measured in MCH at 77 K. It is clear that both phosphorescence bands (^{3}LE, 2.62–2.63 eV) of the conjugates and their donor (2.62 ev) parts closely overlapped with each other, showing that the local triplet state (^{3}LE) is higher in energy than that of ^{1}CT state (Figure 3d). It should be noted that TADF via rISC from the higher-level ^{3}LE to the lower-level ^{1}CT states is also observed (Figure 3d). The energy gap (ΔE_{ST}) between the upper-level triplet (^{3}LE) and lower singlet state (^{1}CT) was determined using the onsets of SS emission (MCH) at RT and phosphorescence spectra (MCH) at 77 K (Figure 3d). The ΔE_{ST} values were found to be 0.11 eV (PTzQ1) and 0.09 eV (PTzQ2), which are consistent for TADF.

Using DF/PF ratio, triplet yield, Φ_{ISC}, is determined and found to be $74 \pm 3\%$ and $77 \pm 2\%$, respectively. The rate of ISC, $k_{ISC} = \frac{\phi_{ISC}}{\tau_{PF}}$ between the ^{1}CT and ^{3}LE, is calculated to be $6.8 \pm 0.3 \times 10^7\ s^{-1}$ and $9.3 \pm 0.4 \times 10^7\ s^{-1}$ ($\tau_{PF} = 10.82$ ns, 8.32 ns). The rate of fluorescence (k_f) and internal conversion rate (k_{IC}) were found to be $0.92 \pm 0.02 \times 10^7$ and $2.1 \pm 0.01 \times 10^7\ s^{-1}$ (PTzQ1) and $1.4 \pm 0.02 \times 10^7$ and $1.3 \pm 0.03 \times 10^7\ s^{-1}$ (PTzQ2). The rate of rISC, $k_{rISC} = \frac{1}{\tau_{DF}} \frac{1}{(1-\phi_{ISC})}$, between the upper-level ^{3}LE and the lower-level ^{1}CT is calculated from the lifetime of the DF component ($\tau_{DF} = 0.42$ µs, $\tau_{DF} = 0.51$ µs) and found to be $0.91 \pm 0.2 \times 10^7$ and $0.85 \pm 0.1 \times 10^7\ s^{-1}$, respectively (Table S5, Supporting Information). These results suggest that k_{ISC} is very high as compared with k_{rISC}, and the sum of the k_F and k_{IC}, indicating that both conjugates show TADF, which is in line with the literature.[5]

2.5.1. Photophysics in Films

To gain knowledge of the emission characteristics, photophysical studies were conducted in rigid poly(methyl methacrylate) (PMMA) matrix (0.5% (w/w)) ($\lambda_{ex} = 340$ nm) for both the conjugates. All the energy of the emission peaks was calculated by taking the onset of the spectra. The absorption spectra of both conjugates showed similar absorption bands (300, 340–350 nm) as compared with those in MCH (Figure S18a, Supporting Information). The donor (PTz) and acceptors (Q1/Q2) also showed absorption bands at 337 nm (broad tail) and 310–350 nm (Figure S16a, Supporting Information). These observations further substantiate our previous argument of electronically decoupled systems (Figure 2, and Table S3, Supporting Information). **Figure 4**a shows that PTzQ1 exhibits predominant lower-energy broad emission bands (^{1}CT) at 563 nm with a weakly intense parent emission peak at 420 nm (^{1}LE, 3.65 eV, $\tau_{avg} = 7.0$ ns), whereas both parent ^{1}LE and ^{1}CT bands in PTzQ2 are almost equally intense, which led to white light emission (^{1}LE; 406 nm, 3.37 eV, $\tau_{avg} = 2.4$ ns; ^{1}CT, 558 nm, 2.63 eV) with Commission Internationale de l'Eclairage (CIE) coordinates of (0.33, 0.35) (Figure 4b, and S18b, Supporting Information). The blue shift of the ^{1}CT band of PTzQ2 as compared with PTzQ1 can be ascribed to the more electron-donating group (–OMe) attached to the LUMO, which modifies the excited electronic levels. The presence of the parent ^{1}LE bands in both conjugates suggests that the radiative recombination from ^{1}LE to the ground state is relatively slow due to rigidity of the host, which can significantly compete with the electron transfer that populates the lower-level ^{1}CT state. PLQY values were determined to be 34% and 28%, respectively, at ambient conditions. Likewise, under nitrogen environment, we found that the emission intensity of the lower-energy bands (λ_{563}, λ_{558}) increases 3.8 times for PTzQ1 and 4.3 times for PTzQ2 at RT, whereas ^{1}LE bands remain unaffected, which confirms that the ^{3}LE state of PTzQ2 is more sensitive to molecular oxygen as compared with the ^{3}LE state of PTzQ1 (Figure S19, Supporting Information). To understand the TADF and RTP features of both compounds, temperature-dependent (210–300 K) PL measurements were undertaken. Temperature-dependent (77–300 K) studies show that the lifetime of the delayed component increases with increase in temperature (Figure 4c), which is fully consistent with the traditional TADF dyes.[5] Further, phosphorescence measurements of both conjugates in the same PMMA films were carried out. Figure 4a,b shows RTP spectra of both compounds at ambient conditions. We found that both conjugates display narrow RTP bands (100 µs detector delay) (FWHM: 90, 88 nm) at ≈530 nm (PTzQ1: 2.627 eV, $\tau_1 = 1.06$ ms; $\tau_2 = 5.48$ ms; PTzQ2: 2.63 eV, $\tau_1 = 1.1$ ms; $\tau_2 = 5.5$ ms), respectively, which are blue shifted (≈25–33 nm) as compared with the ^{1}CT bands (563, 555 nm) (Figure 4d, and S20a, Supporting Information). At 77 K (2.0 ms detector delay), both conjugates exhibit vibrational features of the phosphorescence emission bands

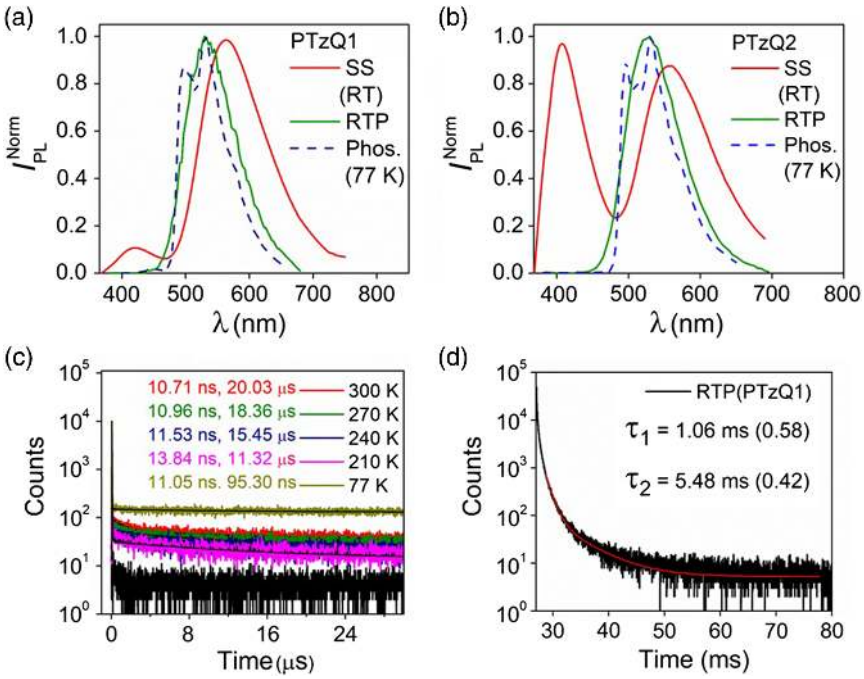

Figure 4. SS and phosphorescence (Phos.) spectra of a) PTzQ1 and b) PTzQ2 at ambient conditions and 77 K (0.5wt% in PMMA). c) Temperature-dependent decay analysis of PTzQ1 and d) RTP decay kinetics of PTzQ1 (0.5wt% in PMMA).

(≈530 nm, 2.63 eV), showing ^{3}LE nature of the triplet state (Figure 4a,b). When we compare this RTP feature with the phosphorescence spectra of the donor (PTz) part, it is clear that the RTP bands of both the conjugates closely overlap with each other (Figure S20b, Supporting Information), which ensures that the PTz part of both conjugates contributes to the ^{3}LE state whereas the ^{1}CT state is populated due to D−A coupling at the excited state. Further, ^{3}LE state populates ^{1}CT via rISC (TADF) and radiates weakly to the ground state as RTP at ambient conditions. The ΔE_{ST} values calculated from the onset of the SS at RT and phosphorescence spectra recorded at 77 K were found to be 0.05 and 0.03 eV for both compounds (Figure 4a,b). The triplet yield (Φ_{isc}) is determined from the PL measurements recorded at both ambient and nitrogen environments. At nitrogen environment, Φ_{isc} values were calculated be 74 ± 1% and 79 ± 2%, respectively, consistent with the previous results in MCH (74 ± 3%, 77 ± 2%, nitrogen environment) (Table S6, Figure S19, Supporting Information). These results are fully consistent with our previous analysis in MCH that an upper-level ^{3}LE triplet state associated with the ^{1}CT emission band is responsible for TADF that occurs via rISC from ^{3}LE to ^{1}CT. To gain more insight into photophysics, time-resolved emission spectra (TRES) of the same PMMA films were measured at ambient conditions (see Supporting Information for details). We confirm in PMMA studies that only one upper-level triplet state (^{3}LE) is involved for both DF and RTP at ambient conditions (Figure S20, S21, Supporting Information). Furthermore, Figure S20c–f, Supporting Information, clearly shows that emission from ^{1}LE state is contributed by both the donor and acceptor parts of PTzQ2, whereas only the donor (PTz) of PTzQ1 contributes to the ^{1}LE emission band (Figure S21a, Supporting Information).

To attain a deeper understanding of their excited-state properties, photophysics of both conjugates (0.5wt%) were analyzed in polar host, bis[2-(di-(phenyl)phosphino)-phenyl]etheroxide (DPEPO) (**Figure 5**). We observed that ^{1}CT emission bands (590, 584 nm) are red shifted, whereas ^{3}LE (PTzQ1: 532 nm, 2.63 eV, $\tau_1 = 2.03$ ms; $\tau_2 = 19.53$ ms; PTzQ2: 532 nm, 2.62 eV, $\tau_1 = 4.05$ ms; $\tau_2 = 23.07$ ms) remained in the same position as compared with PMMA (Figure 5a,b,d, and S23, Supporting Information), indicating that the singlet is more stabilized due to polar host. The FWHM values are found to be 90 and 92 nm, respectively. The PLQY values were determined to be 18 ± 2% and 20 ± 2%, which is consistent with the more stabilized CT state in DPEPO (Table S6, Supporting Information). TADF properties of both conjugates were also measured by lifetime and temperature-dependent analysis (Figure 5c, and S23b, Supporting Information). All the transient decays recorded while decreasing temperature can be fitted by third-order exponential decays, leading to one prompt component and two longer components. At 300 K, the longer components were found to be 1.05 and 3.65 μs (PTzQ1, 590 nm) and 1.06 and 3.99 μs (PTzQ2, 584 nm) (Figure 5c, and S23b, Supporting Information). Surprisingly, we observed an increase in the lifetime of the delayed component (3.65, 3.99 μs) with decrease in temperature. This decrease in lifetime can be attributed to phosphorescence because of which the proportion of the longer component becomes inversely proportional to temperature.[8c] However, a slight increase in the lifetime of the other delayed component from 1.05 to 1.78 μs with decreasing temperature from 300 to 210 K and decrease in the lifetime (1.05 μs) at 77 K means that this component originates from the delayed fluorescence of both the conjugates (Figure 5c).

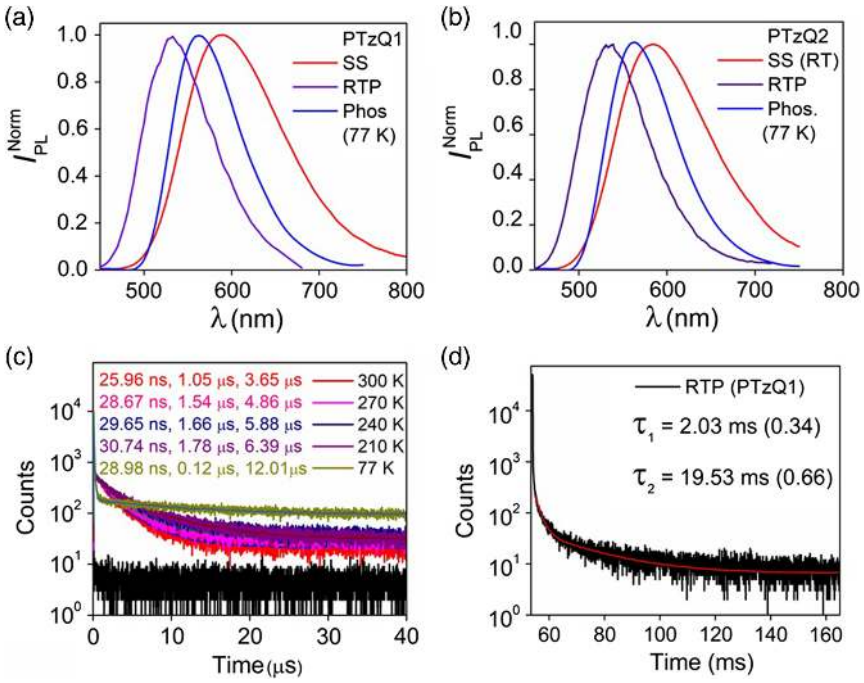

Figure 5. SS and phosphorescence spectra (1 ms detector delay) of a) PTzQ1 and b) PTzQ2 at ambient conditions and 77 K in DPEPO (0.5%). c) Temperature-dependent decay analysis of PTzQ1 and d) RTP decay of PTzQ1 in 0.5% DPEPO.

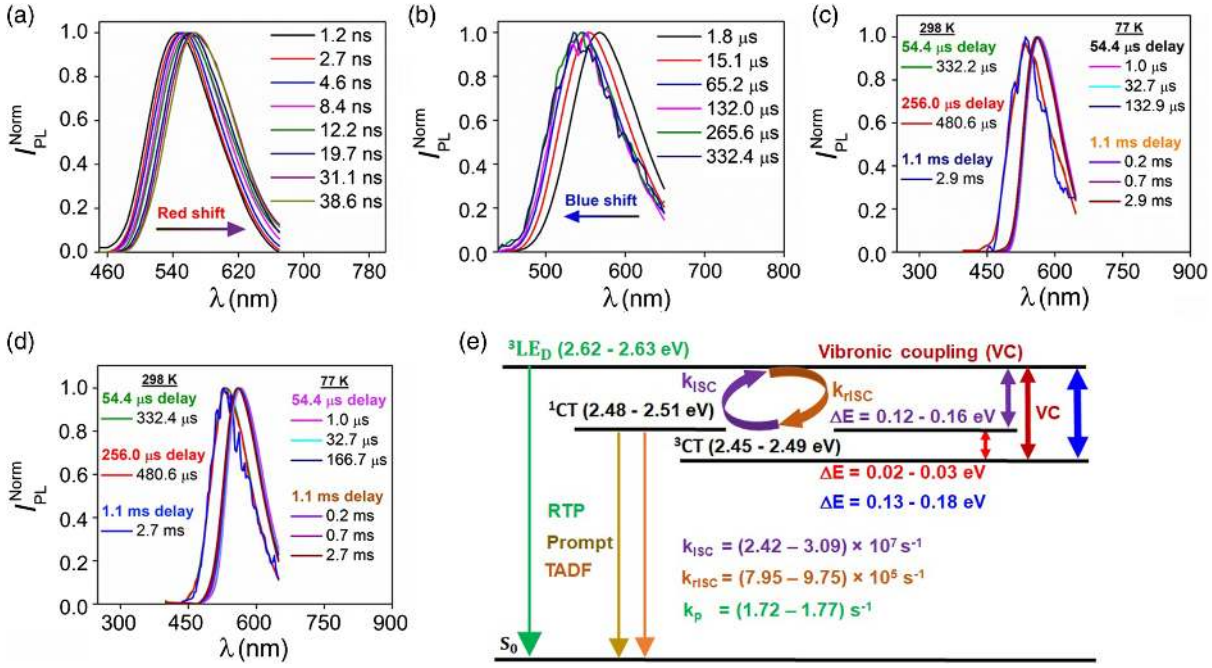

Figure 6. TRES of PTzQ1 a) without detector delay, b) 54.4 μs detector delay at ambient condition, and c) varying detector delays of 54.4 μs (RT and 77 K), 256.0 μs (RT), and 1.1 ms (RT, 77 K). d) TRES of PTzQ2 with varying detector delays of 54.4 μs (RT and 77 K), 256.0 μs (RT), and 1.1 ms (RT, 77 K). e) Jablonski diagram of both PTzQ1 and PTzQ2 (0.5wt% in DPEPO) films.

To gain deeper understanding into exciton dynamics, temperature-dependent (from RT to 77 K) TRES measurements were carried out (**Figure 6**a, and S24, Supporting Information). At RT, at an early time scale of 1.2 ns, a broad emission band at 550 nm was observed for PTzQ1, whereas at a later time scale of 2.7–31.1 ns, this emission band shows red shift (^{1}CT) and after 38.6 ns no more red shift was detected, showing only one emissive state present in this time scale, which resembles the SS spectrum. Furthermore, TRES measurements with 54.4 μs detector delay exhibit a broadband emission feature at (568 nm) early

decay time of 1.8 μs (Figure 6b). At a later time scale of 15.1–332.4 μs (54.4 μs detector delay), this emission band shifts toward a higher-energy region (530 nm, 2.63 eV). After giving 1.1 ms detector delay, the emission band remained at the same position (λ_{530}), which closely matches the RTP spectra recorded at ambient conditions (Figure S25b, Supporting Information). This feature is in good agreement with the TRES results obtained in PMMA films. At 77 K, a similar bathochromic shift of the ^{1}CT band was observed at a time scale of 1.3–38.0 ns (Figure S24b, Supporting Information). Surprisingly, when we record TRES after 54.4 μs detector delay, a new broad emission band (565 nm, 2.64 eV onset) was observed at 1.0 μs time duration, whereas at a later time duration of 32.7–132.9 μs, a hypsochromic shift (5 nm) of the emission band was observed at 560 nm (FWHM = 95 nm) (Figure 6c). After giving 1.1 ms detector delay, this emission band shows no shift at 0.7–2.9 ms time duration, which also matches the phosphorescence spectrum (at 77 K) recorded at 2 ms detector delay (Figure 6b, and S25d, Supporting Information). When we compared the emission band (λ_{560}) with the phosphorescence TRES (RT) recorded at 54.4, 256 μs, and 1.1 ms detector delays with time duration of 332.2, 480.6 μs, and 2.9 ms, we observed that this new triplet state (^{3}CT) was lower in energy than that of ^{3}LE (Figure 5a, 6c). It should be noted that PTzQ2 shows very similar emission dynamics as compared with PTzQ1 (Figure 5b,6c,d, and S24-S25, Supporting Information).

Further photophysical properties of both the conjugates in TCTA (tris(4-carbazoyl-9-ylphenyl)amine (6.0wt%) were investigated. Similar photophysical properties were observed (Figure S26, Supporting Information). The energy differences among the three excited singlet and triplet states were calculated in DPEPO using TRES data recorded at RT and 77 K, which were found to be 0.12–0.16 eV (^{3}LE–^{3}CT), 0.13–0.18 eV (^{3}LE–^{1}CT), and 0.02–0.03 eV (^{3}CT–^{1}CT) (Figure S27, Supporting Information). Quantum yield of fluorescence (Φ_f),phosphorescence (Φ_p), prompt fluorescence (Φ_{PF}), delayed fluorescence (Φ_{DF}), intersystem crossing (Φ_{ISC}), and triplet quantum yield (Φ_t) were calculated for both molecules in DPEPO films (Table S7, Supporting Information). All the radiative and nonradiative rate constants were also calculated (Table S7, Supporting Information). The k_{risc} values were found to be $\approx 7.95 \times 10^5$ and 9.75×10^5 s^{-1}, respectively, which are in good agreement with the literature. Based on these observations, we confirm that an intermediate ^{3}CT state is involved, which may undergo vibronic coupling with the ^{3}LE state, allowing efficient rISC from the ^{3}LE to ^{1}CT due to SOC between them (Figure 6e). Thus, involvement of all the three excited states (^{1}CT, ^{3}CT, ^{3}LE) dictates the underlying mechanism of TADF with RTP.

2.6. OLEDs

The EL characteristics of PTzQ1 and PTzQ2 were tested using the following solution-processed OLED structure, ITO (100 nm)/PEDOT:PSS (30 nm)/EML (≈30 nm)/B3PyMPM (50 nm)/LiF (1 nm)/Al (100 nm), where ITO, PEDOT:PSS, and B3PyMPM represent indium tin oxide, poly(3,4-ethylenedioxythiophene): poly(styrene sulfonate), 4,4′,4″-tris(*N*-carbazolyl)triphenylamine, and 4,6-bis(3,5-di(pyridin-3-yl)phenyl)-2-methylpyrimidine,

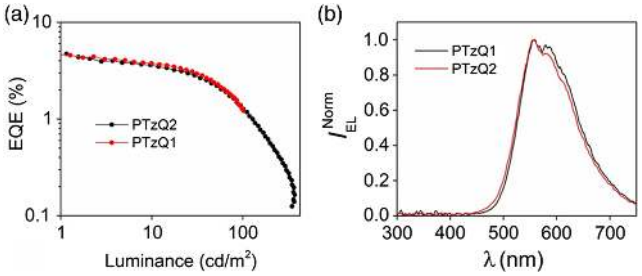

Figure 7. Device performances of PTzQ1- and PTzQ2-based OLEDs: a) EQE–luminance plots and b) EL spectra at 100 cd m^{-2}.

respectively. The energy-level diagram and the schematic representation of the device structure are shown in Figure S28, Supporting Information). The emissive layers (EML) were composed of TADF emitters (6wt% in TCTA) (see supporting information). In the devices, PEDOT:PSS and B3PyMPM were utilized as hole injection and electron transporting layers, respectively. The OLEDs showed appreciable EL properties, which are shown in Table S8, Supporting Information. We have observed almost similar trends for OLEDs based on both emitters in current density–voltage–luminance (*J*–*V*–*L*) behavior (Figure S29, Supporting Information), efficiency, (**Figure 7**a) and spectral emission (Figure 7b). The device turn-on voltage was close to 6.2 V and measured at 1 cd m^{-2}. Maximum EQEs of 4.6% and 4.7% were obtained for PTzQ1- and PTzQ2-based devices, respectively. Given that the blend film PLQYs were determined as 34 ± 4.5% for both compounds in TCTA, a theoretical maximum EQE of 1.7% was expected for a conventional fluorescent emitter, assuming a random dipole orientation of the emitters. The obtained higher EQE values indicate contribution from delayed fluorescence via triplet harvesting, which correlates with our photophysical data. The EQEs of the devices showed extensive roll-off under high current densities. The simple two-layer devices utilized in this work may induce some charge imbalance under high current densities. However, it is not uncommon for solution-processed light-emitting devices to show significant efficiency roll-off.[23] Figure 7b shows the normalized spectral emission of the OLEDs at 100 cd m^{-2}. These spectra confirm that the emission originates only from the respective emitter. Interestingly, EL spectra appear to have two components at 555 and 570 nm unlike most conventional TADF OLEDs. We have found under different voltage biases that the relative contribution from two components remains same (Figure S30, Supporting Information). These results indicate that this class of compound can provide a new route to achieve high-efficiency OLEDs if nonradiative processes are suppressed.

3. Conclusion

We synthesized two new conjugates, PTzQ1 and PTzQ2, in which the donor and acceptor are held in orthogonal orientation. The photophysical studies demonstrate that all three excited states, ^{1}CT, ^{3}CT, and ^{3}LE, play an important role in rISC and thus TADF with green RTP. We identified in both conjugates that the intermediate ^{3}CT state observed in the polar host can be

responsible for vibronic coupling between the ^{3}CT and ^{3}LE that leads to TADF. The presence of the blue-shifted RTP band (TRES measurement), which closely overlaps with the donor phosphorescence spectrum at ambient conditions, confirms that ^{3}LE is higher in energy than that of ^{1}CT. Further, TRES measurements of both conjugates in DPEPO films at 77 K ensure that ^{3}CT is just well below ^{1}CT, resulting in energy ordering of $^3\text{LE} > {}^1\text{CT} > {}^3\text{CT}$ suitable for TADF with green-RTP. From X-ray, CV, and computational analyses, we found that the minimized D−A coupling caused by near-orthogonal orientation of the donor and acceptor parts plays a key role in the TADF process. Solution-processed OLED devices have shown efficiency close to their theoretical maximum. This study may open a door to understand the underlying photophysics of TADF with RTP. Further study of such organic conjugates having RTP with the TADF feature and reduced nonradiative rates promising for device fabrication is under way in our laboratory.

Supporting Information

Supporting Information is available from the Wiley Online Library or from the author.

Acknowledgements

This article is dedicated to Professor Rupamanjari Ghosh on the occasion of her 64th birthday. D. R. is grateful to the Board of Research and Nuclear Science (BRNS) (file no. 37(3)/14/08-2018-BRNS/37130), DAE, and Department of Science and Technology (DST) (file no: EEQ/2020/000029). N. A. thanks SNU for fellowship. The authors also thank Department of Industry, Innovation and Science (AISRF53765) for financial support.

Conflict of Interest

The authors declare no conflict of interest.

Data Availability Statement

CCDC 2034110 and 2034112 contains the supplementary crystallographic data for this paper. These data can be obtained free of charge from The Cambridge Crystallographic Data Centre via www.ccdc.cam.ac.uk/data_request/cif.

Keywords

donor (D)−acceptors (A), electroluminescence, organic light-emitting diodes, room-temperature phosphorescence, thermally activated delayed fluorescence

Received: January 13, 2021
Revised: January 30, 2021
Published online: March 8, 2021

[1] a) M. Pope, H. Kallmann, P. Magnante, *J. Chem. Phys.* **1963**, *38*, 2042; b) L. J. Rothberg, A. J. Lovinger, *J. Mater. Res.* **1996**, *11*, 3174; c) C. W. Tang, S. A. VanSlyke, *Appl. Phys. Lett.* **1987**, *51*, 913; d) T. Tsutsui, S. Saito, in *Intrinsically Conducting Polymers: An Emerging Technology*, Springer, New York **1993**, pp. 123–124.

[2] a) M. Baldo, S. Lamansky, P. Burrows, M. Thompson, S. Forrest, *Appl. Phys. Lett.* **1999**, *75*, 4; b) M. A. Baldo, D. F. O'Brien, Y. You, A. Shoustikov, S. Sibley, M. E. Thompson, S. R. Forrest, *Nature*, **1998**, *395*, 151; c) I. V. Khudyakov, Y. A. Serebrennikov, N. J. Turro, *Chem. Rev.* **1993**, *93*, 537; d) N. J. Turro, V. Ramamurthy, V. Ramamurthy, J. C. Scaiano, in *Principles of Molecular Photochemistry: An Introduction*, University Science Books, California **2009**; e) Q. Zhao, F. Li, C. Huang, *Chem. Soc. Rev.* **2010**, *39*, 3007. f) H. F. Higginbotham, M. Okazaki, P. D. Silva, S. Minakata, Y. Takeda, P. Data, *ACS Appl. Mater. Interfaces* **2021**, *13*, 2899.

[3] a) J. Lakowicz, in *Principles of Fluorescence Spectroscopy*, Springer, New York **2006**, pp. 158–204; b) T. Sajoto, P. I. Djurovich, A. Tamayo, M. Yousufuddin, R. Bau, M. E. Thompson, R. J. Holmes, S. R. Forrest, *Inorg. Chem.* **2005**, *44*, 7992; c) H. Yersin, in *Highly Efficient OLEDs with Phosphorescent Materials*, John Wiley & Sons, Hoboken, NJ **2008**.

[4] S. King, M. Cass, M. Pintani, C. Coward, F. Dias, A. Monkman, M. Roberts, *J. Appl. Phys.* **2011**, *109*, 074502.

[5] a) F. B. Dias, T. J. Penfold, A. P. Monkman, *Methods. Appl. Fluoresc.* **2017**, *5*, 012001; b) G. A. Sommer, L. N. Mataranga-Popa, R. Czerwieniec, T. Hofbeck, H. H. H. Homeier, T. J. J. Müller, H. Yersin, *J. Phys. Chem. Lett.* **2018**, *9*, 3692; c) H. Uoyama, K. Goushi, K. Shizu, H. Nomura, C. Adachi, *Nature* **2012**, *492*, 234; d) Q. Zhang, J. Li, K. Shizu, S. Huang, S. Hirata, H. Miyazaki, C. Adachi, *J. Am. Chem. Soc.* **2012**, *134*, 14706.

[6] a) C. M. Marian, *J. Phys. Chem. C* **2016**, *120*, 3715; b) B. T. Lim, S. Okajima, A. Chandra, E. Lim, *Chem. Phys. Lett.* **1981**, *79*, 22; c) J. Gibson, A. P. Monkman, T. J. Penfold, *Chem. Phys. Chem.* **2016**, *17*, 2956; d) M. K. Etherington, J. Gibson, H. F. Higginbotham, T. J. Penfold, A. P. Monkman, *Nat. Commun.* **2016**, *7*, 13680; e) F. B. Dias, J. Santos, D. R. Graves, P. Data, R. S. Nobuyasu, M. A. Fox, A. S. Batsanov, T. Palmeira, M. N. Berberan-Santos, M. R. Bryce, *Adv. Sci.* **2016**, *3*, 1600080; f) X.-K. Chen, S.-F. Zhang, J.-X. Fan, A.-M. Ren, *J. Phys. Chem. C* **2015**, *119*, 9728.

[7] a) Y. Xu, C. Wang, X. Zhou, J. Zhou, X. Guo, X. Liang, D. Hu, F. Li, D. Ma, Y. Ma, *J. Phys. Chem. Lett.* **2019**, *10*, 6878; b) Y. Wada, H. Nakagawa, S. Matsumoto, Y. Wakisaka, H. Kaji, *Nat. Photonics* **2020**, *14*, 643.

[8] a) N. A. Kukhta, M. R. Bryce, *Mater. Horizons* **2021**, *8*, 33; b) I. Bhattacharjee, N. Acharya, D. Ray, *Chem. Commun.* **2019**, *55*, 1899; c) I. Bhattacharjee, N. Acharya, H. Bhatia, D. Ray, *J. Phys. Chem. Lett.* **2018**, *9*, 2733; d) H. Bhatia, D. Ray, *Mater. Adv.* **2020**, *1*, 1858; e) J. Gierschner, S. K. Behera, S. Y. Park, *Angew. Chem. Int. Ed.* **2020**, https://onlinelibrary.wiley.com/doi/abs/10.1002/anie.202009789.

[9] a) C. Salas Redondo, P. Kleine, K. Roszeitis, T. Achenbach, M. Kroll, M. Thomschke, S. Reineke, *J.Phys. Chem. C* **2017**, *121*, 14946; b) I. Bhattacharjee, N. Acharya, S. Karmakar, D. Ray, *J. Phys. Chem. C* **2018**, *122*, 21589.

[10] a) M. S. Kwon, D. Lee, S. Seo, J. Jung, J. Kim, *Angew. Chem. Int. Ed.* **2014**, *53*, 11177; b) H. Bhatia, D. Ray, *J. Phys. Chem. C* **2019**, *123*, 22104; c) H. Bhatia, I. Bhattacharjee, D. Ray, *J. Phys. Chem. Lett.* **2018**, *9*, 3808.

[11] a) J. Zhang, E. Sharman, L. Yang, J. Jiang, G. Zhang, *J. Phys. Chem. C* **2018**, *122*, 25796; b) Z. An, C. Zheng, Y. Tao, R. Chen, H. Shi, T. Chen, Z. Wang, H. Li, R. Deng, X. Liu, *Nat. Mater.* **2015**, *14*, 685.

[12] a) D. Lee, O. Bolton, B. C. Kim, J. H. Youk, S. Takayama, J. Kim, *J. Am. Chem. Soc.* **2013**, *135*, 6325; b) S. Hirata, K. Totani, J. Zhang, T. Yamashita, H. Kaji, S. R. Marder, T. Watanabe,

C. Adachi, *Adv. Funct. Mater.* **2013**, *23*, 3386; c) H. A. Al-Attar, A. P. Monkman, *Adv. Func. Mater.* **2012**, *22*, 3824.
[13] I. Bhattacharjee, S. Hirata, *Adv. Mater.* **2020**, *32*, 2001348.
[14] X. Sun, B. Zhang, X. Li, C. O. Trindle, G. Zhang, *J. Phys. Chem. A* **2016**, *120*, 5791.
[15] J. S. Ward, R. S. Nobuyasu, A. S. Batsanov, P. Data, A. P. Monkman, F. B. Dias, M. R. Bryce, *Chem. Commun.* **2016**, *52*, 2612.
[16] L. Zhan, Z. Chen, S. Gong, Y. Xiang, F. Ni, X. Zeng, G. Xie, C. Yang, *Angew. Chem.* **2019**, *131*, 17815.
[17] a) T. Serevičius, T. Bučiūnas, J. Bucevičius, J. Dodonova, S. Tumkevičius, K. Kazlauskas, S. Juršėnas, *J. Mater. Chem. C* **2018**, *6*, 11128; b) J. S. Ward, R. S. Nobuyasu, M. A. Fox, A. S. Batsanov, J. Santos, F. B. Dias, M. R. Bryce, *J. Org. Chem.* **2018**, *83*, 14431; c) P. Data, M. Okazaki, S. Minakata, Y. Takeda, *J. Mater. Chem. C* **2019**, *7*, 6616.
[18] Y. Takeda, T. Kaihara, M. Okazaki, H. Higginbotham, P. Data, N. Tohnai, S. Minakata, *Chem. Commun.* **2018**, *54*, 6847.
[19] a) S. Zhang, M. Hosaka, T. Yoshihara, K. Negishi, Y. Iida, S. Tobita, T. Takeuchi, *Cancer Res.* **2010**, *70*, 4490; b) G. Zhang, G. M. Palmer, M. W. Dewhirst, C. L. Fraser, *Nat. Mater.* **2009**, *8*, 747.
[20] M. J. Frisch, G. W. Trucks, H. B. Schlegel, G. E. Scuseria, M. A. Robb, J. R. Cheeseman, G. Scalmani, V. Barone, B. Mennucci, G. A. Petersson, H. Nakatsuji, M. Caricato, X. Li, H. P. Hratchian, A. F. Izmaylov, J. Bloino, G. Zheng, J. L. Sonnenberg, M. Hada, M. Ehara, K. Toyota, R. Fukuda, J. Hasegawa, M. Ishida, T. Nakajima, Y. Honda, O. Kitao, H. Nakai, T. Vreven, J. A. Montgomery, Jr., et al., *Gaussian 09, Revision D.01*, Gaussian Inc, Wallingford CT **2013**.
[21] M. Szymańska, I. Majerz, *J. Mole. Str.* **2020**, *1200*, 127095.
[22] R. L. Martin, *J. Chem. Phys.* **2003**, *118*, 4775.
[23] a) X. Liu, B. Yao, Z. Zhang, X. Zhao, B. Zhang, W.-Y. Wong, Y. Cheng, Z. Xie, *J. Mater. Chem. C* **2016**, *4*, 5787; b) S. C. Lo, R. N. Bera, R. E. Harding, P. L. Burn, I. D. W. Samuel, *Adv. Func. Mater.* **2008**, *18*, 3080.